24. Conway, S. & Glasser, B. Density waves and coherent structures in granular Couette flows. *Phys. Fluids* **16**, 509–529 (2004).

25. Ottino, J. M. & Khakhar, D. V. Mixing and segregation of granular materials. *Annu. Rev. Fluid Mech.* **32**, 55–91 (2000).

26. Bridgwater, J. Fundamental powder mixing mechanisms. *Powder Technol.* **15**, 215–236 (1976).

27. Joseph, D. D., Wang, J., Bai, R., Yang, B. H. & Hu, H. H. Particle motion in a liquid film rimming the inside of a partially filled rotating cylinder. *J. Fluid Mech.* **496**, 139–163 (2003).

28. Matson, W. R., Ackerson, B. J. & Tong, P. Pattern formation in a rotating suspension of non-Brownian settling particles. *Phys. Rev. E* **67**, 050301 (2003).

29. Shinbrot, T. & Muzzio, F. Nonequilibrium patterns in granular mixing and segregation. *Physics Today* **53**, 25–30 (2000).

....

Complete photo-fragmentation of the deuterium molecule

T. Weber[1,2,3], **A. O. Czasch**[1], **O. Jagutzki**[1], **A. K. Müller**[1], **V. Mergel**[1], **A. Kheifets**[4], **E. Rotenberg**[2], **G. Meigs**[2], **M. H. Prior**[2], **S. Daveau**[2], **A. Landers**[5], **C. L. Cocke**[3], **T. Osipov**[3], **R. Díez Muiño**[6], **H. Schmidt-Böcking**[1] & **R. Dörner**[1]

[1]*Institut für Kernphysik, Universität Frankfurt, D 60486 Frankfurt, Germany*
[2]*Lawrence Berkeley National Laboratory, Berkeley, California 94720, USA*
[3]*Department of Physics, Kansas State University, Manhattan, Kansas 66506, USA*
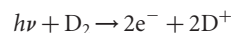[4]*Research School of Physical Sciences and Engineering, Australian National University, Canberra ACT 0200, Australia*
[5]*206 Allison Laboratory, Auburn University, Alabama 36849 5311, USA*
[6]*Donostia International Physics Center and Unidad de Fisica de Materiales, 20 018 Donostia-San Sebastian, Spain*

....

All properties of molecules—from binding and excitation energies to their geometry—are determined by the highly correlated initial-state wavefunction of the electrons and nuclei. Details of these correlations can be revealed by studying the break-up of these systems into their constituents. The fragmentation might be initiated by the absorption of a single photon[1–6], by collision with a charged particle[7,8] or by exposure to a strong laser pulse[9,10]:

if the interaction causing the excitation is sufficiently understood, the fragmentation process can then be used as a tool to investigate the bound initial state[11,12]. The interaction and resulting fragment motions therefore pose formidable challenges to quantum theory[13–15]. Here we report the coincident measurement of the momenta of both nuclei and both electrons from the single-photon-induced fragmentation of the deuterium molecule. The results reveal that the correlated motion of the electrons is strongly dependent on the inter-nuclear separation in the molecular ground state at the instant of photon absorption.

Small systems of Coulomb interacting particles such as the helium atom or the hydrogen molecule have been models for quantum theory since its early days. However, despite 80 years of theoretical attention, nearly exact calculations for such systems are available only for bound states. On the experimental side, tests of these calculations are based largely on level energies or single-particle momentum distributions. Very promising and challenging new classes of experiments are those that achieve a complete description of the outcome after excitation of the ground state to an unbound continuum. The momenta—that is, the set of vectors—of all fragments of the break-up of an atom or molecule can be measured in coincidence with high precision by using state-of-the-art imaging and timing techniques[16]. These asymptotic many-particle momentum distributions are determined by the interaction inducing the fragmentation, the bound initial state from which it emerged, and interactions between the outgoing particles. Thus, experimentalists find it useful to keep the interaction process as simple as possible and to choose a geometry in which final state interactions are negligible. In the present study we used the absorption of a single photon to fragment the deuterium molecule:

$$h\nu + D_2 \rightarrow 2e^- + 2D^+$$

Because of the heavy masses of the nuclei, their initial motion in the continuum can be assumed to be the same as in the ground state at the instant of the electronic transition (Born–Oppenheimer approximation). Once the electrons have left the system, the motion of the nuclei is determined solely by their Coulomb repulsion; they accelerate to a kinetic energy release (KER) that corresponds to the Coulomb potential associated with their initial separation. Quantum mechanically, one maps the nuclear vibrational wavefunction onto the Coulomb potential to yield a KER spectrum. Inverting this process determines the squared nuclear vibrational wavefunction from the measured KER spectrum[17]. Furthermore, by selecting events that occur within a fixed subregion in the KER spectrum,
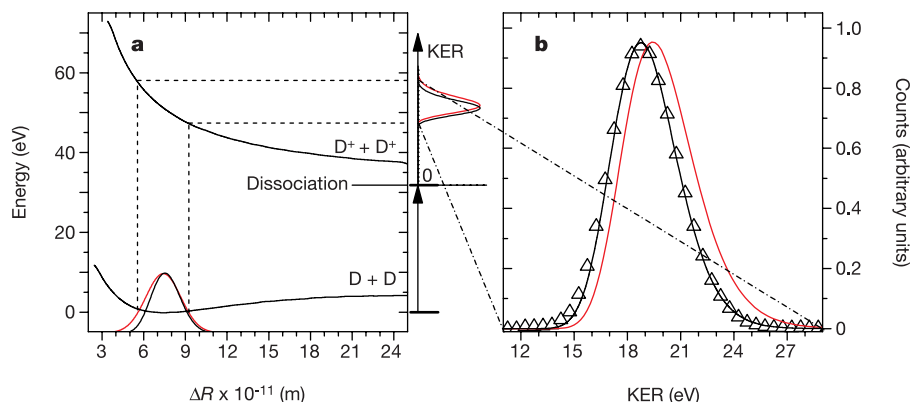

Figure 1 Mapping of the ground-state distribution of inter-nuclear distances to the kinetic energy in the final state. Determination of the inter-nuclear distance ΔR in the ground state of D_2 by measuring the KER after double ionization with linear polarized light of 75.5 eV. In panel **a** the squared ground-state wavefunction is mirrored at the repulsive $D^+ + D^+$ potential curve onto the KER (shown as an enlargement in panel **b**): the red curves show the prediction starting from a harmonic oscillator potential; the black curves show the same from a Morse potential. The open triangles are the experimental measurements (the standard deviation of the mean value is smaller than the size of the triangles).

molecules are sampled whose corresponding inter-nuclear distance is defined much more precisely than the full extent of the initial nuclear wavefunction. This allows us to show how the electronic continuum momentum distribution depends on the inter-nuclear separation in the molecule and its orientation with respect to the photon polarization.

Multi-particle coincidence experiments have become possible with the advent of modern imaging techniques based on micro-channel plate multipliers combined with high-resolution time-of-flight measurements[18–21]. In brief, inside our momentum spectrometer, a supersonic jet of D_2 gas was crossed with the linear polarized photon beam from the Lawrence Berkeley National Laboratory Advanced Light Source (D_2 provides higher target density than a comparable H_2 gas jet, and data are less contaminated by random coincidences from background water). The electrons and ions created in the intersection of the photons with the jet are guided by a combination of homogeneous electric and parallel magnetic fields onto channel plate detectors. For each particle, the
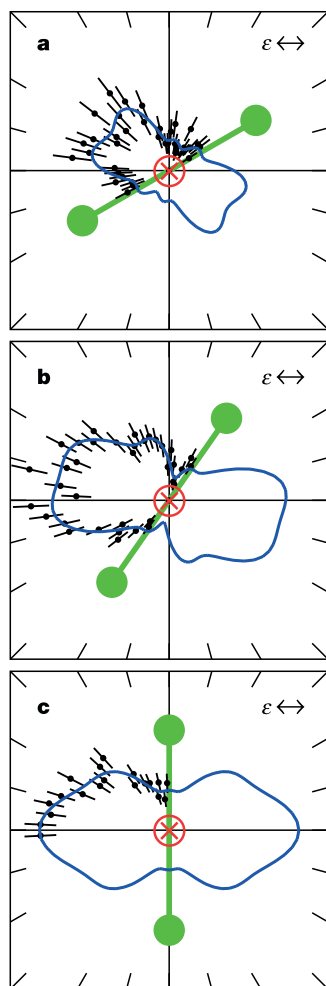
position of impact and the time of flight to the detector are registered. From these values and the geometry and fields, the momentum vectors of all particles from each fragmentation event can be calculated. The validity and sensitivity of the mapping of the ground-state distribution of inter-nuclear distances to the KER is shown in Fig. 1. The red line shows the squared nuclear wavefunction obtained when approximating a D_2 potential curve by a harmonic oscillator with the correct vibration frequency and equilibrium distance; the black curve shows the calculation with
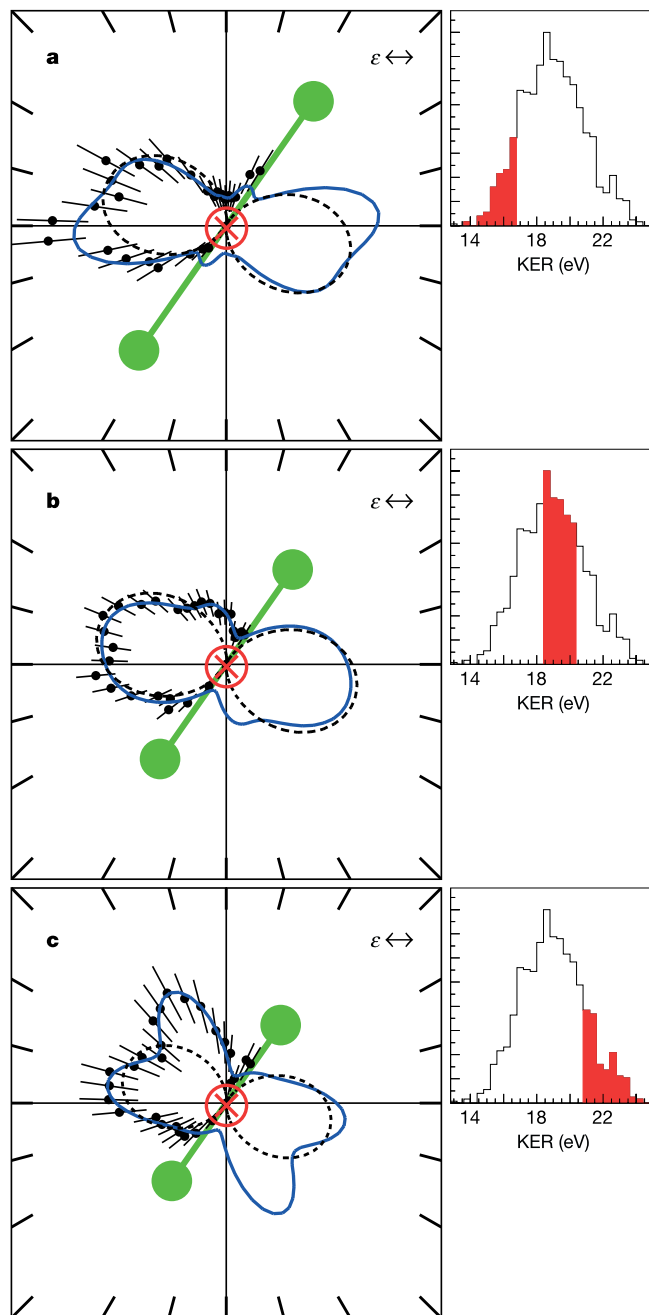

Figure 2 Angular distribution in the non-coplanar frame as a function of molecular orientation. Shown is the angular distribution of one electron (black dots with error bars indicating the standard deviation of the mean value) in the plane of the molecular axis (green barbell) and the electric field vector of the linear polarized light ε (horizontal double arrow) for a photon energy of 75.5 eV. In panel **a** the angle between the molecule and the polarization axis is 30°, whereas it is 55° in **b** and 90° in **c**. The other electron moves orthogonally out of the plane towards the observer (the red circled cross). Each electron has 12.25 eV energy. Because any half-plane is indistinguishable from its inverted complement, we place all data into one half-plane even though we collect ions and electrons in all 4π of laboratory space. The blue solid lines show a fit with spherical harmonics ($l \in [1,4]$, $m \in [0,1]$).

Figure 3 Angular distribution in the non-coplanar frame as a function of KER. Details are as in Fig. 2, but here the molecular axis is fixed at 55° as indicated while the KER varies between panels **a**, **b** and **c** as shown in the insets to the right. High KER corresponds to small inter-nuclear distances ΔR at the instant of photon absorption as described in Fig. 1 (indicated by the varying length of the green 'barbell' in each panel). The blue solid lines show a fit with spherical harmonics ($l \in [1,4]$, $m \in [0,1]$). The dashed black lines represent the result from a single centre expansion of the molecular ground state and a CCC expansion of the final two-electron continuum.

an improved wavefunction obtained from a much more accurate Morse potential.

In Fig. 2 we illustrate the dependence of angular distributions of coincident electrons on the molecular orientation. In this figure the molecular axis, the light polarization axis ε and one of the electrons are restricted to one plane. The momentum vector of the second electron is fixed perpendicular to that plane, pointing towards the observer. By keeping the angle between the two electrons constant at $90°$, we expect minimal influence and variation of the electron–electron interaction in the final state. For other geometries we find that the angular distributions are almost completely dominated by the interplay between electron–electron repulsion, angular momentum and parity selection rules[14,22].

An atomic photo-ionization cross-section can be described by a dipole distribution with its symmetry axis in the direction of the polarization of the incoming photon. In contrast, Fig. 2, for the molecular case, shows a strong dependence of the angular distribution of the electrons on the molecular orientation, showing the importance of this new internal reference axis. Whereas the light field attempts to drive electrons towards a dipole pattern keyed to its polarization axis, the two-body Coulomb potential of the molecule tends to favour electrons escaping perpendicular to its axis. Calculations with a correlated final state that includes all two-body interactions (except the inter-nuclear repulsion) contradict this behaviour (see ref. 23). Furthermore, the distribution is not describable by a pure dipole shape; it shows additional small lobes (see Fig. 2b, c) indicating that higher-angular-momentum components are present. A possible reason for the preferred emission perpendicular to the molecular axis could be the ground-state electron momentum distribution in the molecule. Because the electronic wavefunction is elongated along the inter-nuclear axis in configuration space, the momentum space wavefunction—that is, the Fourier transform—forms a peak perpendicular to the molecular axis. The photo-ionization probes the momentum-space wavefunction; indeed, the photo-ionization matrix element in the high-energy limits corresponds to the Fourier transform of the initial state[23]. In contrast, a description of the ionization process in terms of diffraction of an outgoing electron by the two centres of the potential can yield similar complex angular distribution patterns. From this one might expect that these emission patterns of the photo double ionization shown in Fig. 2 can be described by the single ionization of a D_2^+ ion. Despite these seemingly reasonable qualitative ideas, we show below that this approach is not appropriate.

A key result of our experiment is shown in Fig. 3. The geometry is the same as in Fig. 2, but here the plots are made for selected regions in the KER spectrum. For the smallest KER (that is, the largest separation), the angular distribution resembles a helium-like dipole pattern, in that it is aligned mainly along the polarization axis (see Fig. 3a). For the smallest inter-nuclear separation (Fig. 3c) the emission pattern is essentially orthogonal to the molecular axis and the distribution changes from a dipole to a four-lobed pattern, indicating that higher-angular-momentum components are involved. What is the physical origin of these observations? First, we exclude interference modulations from simple two-centre diffraction, because here the wavelengths of the electrons are four to six times the inter-nuclear separation. Second, whereas a multiple scattering of the photoelectron wave could lead to a variation of the angular distributions, as is predicted and observed for K-shell ionization of the CO molecule for instance[24], investigations on H_2, applying the method described in ref. 25, show that this effect, as a function of the inter-nuclear separation ΔR, is rather small. This is because the protons are relatively weak scattering centres and the long wavelength of the photoelectrons would require long paths within the molecular potential. A remaining possibility might be found in the initial-state electronic wavefunction.

A calculation based on an appropriate two-electron equilibrium initial state is included in Fig. 3b. The corresponding experimental data show a mixture of patterns similar to the dipole distribution of Fig. 3a and the four-lobed structure of Fig. 3c. A simple model[26,27], in which a pair of photo-ionization amplitudes f_Σ and f_Π are introduced for light polarization parallel (Σ transition) and perpendicular (Π transition) to the molecular axis ionizing the molecule, is shown as the dashed black line. To evaluate the amplitudes f_Σ and f_Π we used a single-centre expansion of the H_2 ground state[28] and a convergent close-coupling (CCC) expansion of the final two-electron state in the field of a point-like charge $Z = 2$ (ref. 29). This calculation, neglecting two-centre electron–nuclei interaction in the final state, yields only the dipole pattern. The difference between this result and the observations reveals the complex diffraction of the outgoing electron wave from a highly correlated two-electron initial state. Although they reproduce a decrease in magnitude, the CCC calculations corresponding to the kinematics of Fig. 3a, c based on single-centre Slater-type orbitals for different inter-nuclear distances[30] (shown also as dashed black lines) do not differ greatly from the result shown for the equilibrium state in Fig. 3b. Apparently this kind of initial-state function is not as sensitive to small changes in ΔR as the experimental data seem to require.

Thus we see complex structures in the electronic angular distribution that depend strongly on the molecular orientation and the inter-nuclear separation. The angular distributions, apparently highly influenced by an appropriate initial-state wavefunction, diffraction and electron–electron correlation, show behaviour that is both unexpected and not yet understood. Our results are highly sensitive and direct tests of the initial-state wavefunction and its correlation effects. An intricate calculation to address our observations is highly desirable. A complete treatment of the break-up of this fundamental molecule would mark a significant step towards understanding the quantum dynamics of many-particle systems, a subject central to most physical and chemical processes. □

1. Kossmann, H., Schwarzkopf, O., Kämmerling, B. & Schmidt, V. Unexpected behavior of double photoionization in H_2. *Phys. Rev. Lett.* **63**, 2040–2043 (1989).
2. Dujardin, G., Besnard, M. J., Hellner, L. & Malinovitch, Y. Double photoionization of H_2: An experimental test of electronic-correlation models in molecules. *Phys. Rev. Lett.* **35**, 5012–5019 (1987).
3. Reddish, T. J., Wightman, J. P., MacDonald, M. A. & Cvejanovic, S. Triple differential cross section measurements for double photoionization of D_2. *Phys. Rev. Lett.* **79**, 2438–2441 (1997).
4. Wightman, J., Cvejanovic, S. & Reddish, T. J. (γ,2e) cross section measurements of D_2 and He. *J. Phys. B* **31**, 1753–1764 (1998).
5. Seccombe, D. P. *et al.* Photodouble ionization differential cross sections for D_2 with various electron energy sharing conditions. *J. Phys. B* **35**, 3767–3780 (2002).
6. Dörner, R. *et al.* Double photoionization of spatially aligned D_2. *Phys. Rev. Lett.* **81**, 5776–5779 (1998).
7. Afaneh, F. *et al.* Must saddle point electrons always ride on the saddle? *J. Phys. B.* **35**, L229–L235 (2002).
8. Wood, R. M., Edwards, A. K. & Steuer, M. F. Dissociative ionization of H_2 and D_2 produced by bombardment with fast He^+ ions. *Phys. Rev. A* **4**, 1433–1437 (1977).
9. Staudte, A. *et al.* Observation of a nearly isotropic, high-energy Coulomb explosion group in the fragmentation of D_2 by short laser pulses. *Phys. Rev. A.* **65**, 020703-1–020703-4 (2002).
10. Rottke, H. *et al.* Coincident fragment detection in strong field photoionization and dissociation of H_2. *Phys. Rev. Lett.* **89**, 013001-1–013001-4 (2002).
11. Moshammer, R. *et al.* The dynamics of target ionization by fast highly charged projectiles. *Nucl. Instr. Meth. Phys. Res. B* **107**, 62–66 (1996).
12. Levin, V. G., Neudatchin, V. G., Pavlitchankov, A. V. & Smirnov, Yu. F. A study of the electron correlations in the H_2 molecule using the double photoionisation process (γ,2e). *J. Phys. B* **17**, 1525–1536 (1984).
13. Rescigno, T. N., Baertschy, M., Isaacs, W. A. & McCurdy, C. W. Collisional breakup in a quantum system of three charged particles. *Science* **286**, 2474–2479 (1999).
14. Weber, T. *et al.* Fully differential cross sections for photo-double-ionization of D_2. *Phys. Rev. Lett.* **92**, 163001-1–163001-4 (2004).
15. Briggs, J. & Schmidt, V. Differential cross section for photo-double-ionization of the helium atom. *J. Phys. B* **33**, R1–R48 (2000).
16. Dörner, R. *et al.* Photo-double-ionization of He: Fully differential and absolute electronic and ionic momentum distributions. *Phys. Rev. A* **57**, 1074–1090 (1998).
17. Le Rouzo, H. Double photoionization of molecular hydrogen: A theoretical study including the nuclear dissociation. *Phys. Rev. A* **37**, 1512–1523 (1988).
18. Dörner, R. *et al.* Cold target recoil ion momentum spectroscopy: a 'momentum microscope' to view atomic collision dynamics. *Phys. Rep.* **330**, 95–192 (2000).
19. Ullrich, J. *et al.* Recoil-ion and electron momentum spectroscopy: reaction-microscopes. *Rep. Prog. Phys.* **66**, 1463–1545 (2003).

20. Weber, T. *et al.* Correlated electron emission in multiphoton double ionization. *Nature* **405**, 658–661 (2000).

21. Schulz, M. *et al.* Three-dimensional imaging or atomic four-body processes. *Nature* **422**, 48–50 (2003).

22. Walter, M. & Briggs, J. S. Selection rules and isotope effects in the full fragmentation of the hydrogen molecule. *Phys. Rev. Lett.* **85**, 1630–1633 (2000).

23. Walter, M. & Briggs, J. S. Photo-double ionization of molecular hydrogen. *J. Phys. B* **32**, 2487–2501 (1999).

24. Weber, T. *et al.* Auger electron emission from fixed-in-space CO. *Phys. Rev. Lett.* **90**, 153003-1–153003-4 (2003).

25. Díez Muiño, R., Rolles, D., de Abajo, F. J. G., Fadley, C. S. & Hove, M. A. V. Angular distribution of the electrons photoemitted from core levels of oriented diatomic molecules: multiple scattering theory in non-spherical potentials. *J. Phys. B* **35**, L359–L365 (2002).

26. Feagin, J. M. A helium-like description of molecular hydrogen photo-double ionization. *J. Phys. B* **31**, L729–L736 (1998).

27. Reddish, T. J. & Feagin, J. M. Photo double ionization of molecular deuterium. *J. Phys. B* **32**, 2473–2486 (1999).

28. Joy, H. W. & Parr, R. G. A one-center wave function for the hydrogen molecule. *J. Chem. Phys.* **28**, 448–453 (1958).

29. Kheifets, A. S. & Bray, I. Application of the CCC method to the calculation of helium-photoionization triply differential cross sections. *J. Phys. B* **31**, L447–L453 (1998).

30. Hayes, E. F. Accurate single-center expansions using Slater type orbitals: hydrogen molecule. *J. Chem. Phys.* **46**, 4004–4008 (1967).

....

Ecosystem carbon storage in arctic tundra reduced by long-term nutrient fertilization

Michelle C. Mack[1]*, **Edward A. G. Schuur**[1]*, **M. Syndonia Bret-Harte**[2], **Gaius R. Shaver**[3] & **F. Stuart Chapin III**[2]

[1]*Department of Botany, University of Florida, Gainesville, Florida 32611, USA*
[2]*Institute of Arctic Biology, University of Alaska Fairbanks, Fairbanks, Alaska 99775, USA*
[3]*The Ecosystems Center, Marine Biological Laboratory, Woods Hole, Massachusetts 02543, USA*

* These authors contributed equally to this work
....

Global warming is predicted to be most pronounced at high latitudes, and observational evidence over the past 25 years suggests that this warming is already under way[1]. One-third of the global soil carbon pool is stored in northern latitudes[2], so there is considerable interest in understanding how the carbon balance of northern ecosystems will respond to climate warming[3,4]. Observations of controls over plant productivity in tundra and boreal ecosystems[5,6] have been used to build a conceptual model of response to warming, where warmer soils and increased decomposition of plant litter increase nutrient availability, which, in turn, stimulates plant production and increases ecosystem carbon storage[6,7]. Here we present the results of a long-term fertilization experiment in Alaskan tundra, in which increased nutrient availability caused a net ecosystem loss of almost 2,000 grams of carbon per square meter over 20 years. We found that annual aboveground plant production doubled during the experiment. Losses of carbon and nitrogen from

deep soil layers, however, were substantial and more than offset the increased carbon and nitrogen storage in plant biomass and litter. Our study suggests that projected release of soil nutrients associated with high-latitude warming may further amplify carbon release from soils, causing a net loss of ecosystem carbon and a positive feedback to climate warming.

The effects of climate warming on ecosystem carbon (C) storage remain uncertain. Despite the low temperatures at high latitudes, C storage in tundra and boreal ecosystems is thought to be constrained ultimately by carbon–nutrient interactions because plant production is usually nitrogen (N)-limited[6,7]. As soils warm in response to climate change, nutrient mineralization from soil organic matter is expected to increase[8,9], which should, in turn, increase plant production. Total ecosystem C storage, however, depends on the balance between production and decomposition, and the relationship between nutrient availability and decomposition remains uncertain.

In ecosystems at lower latitudes, natural and manipulated nutrient concentrations have had a positive, a negative, or no effect on the decomposition of litter and soil organic C (SOC)[10–13]. This variable response probably reflects ecosystem differences in form and quality of litter and SOC, but the regulatory mechanism for this is poorly understood[13]. High-latitude ecosystems are unusual because they store a larger proportion of total ecosystem C in soil compared with temperate and tropical ecosystems[14]. In arctic tundra, as much as 90% of the total ecosystem C resides in organic horizons and frozen mineral soils[15]. Thus, the response of SOC to changes in nutrient availability will play a critical role in determining net ecosystem C balance in a changing climate.

Previous results from nutrient manipulations suggested that increased nutrient availability should increase the total C storage in tundra ecosystems[2,9,15,16]. Nutrient addition greatly increases C stored aboveground by stimulating plant productivity and by shifting species composition from slow-growing species to more productive shrubs that accumulate C in long-lived woody biomass[4,17–19]. In addition, leaf, root and stem litter from shrubs decomposes more slowly than the graminoid-dominated litter they replace[9], so conversion to shrub tundra was thought to slow decomposition and increase ecosystem C accumulation[19]. However, these inferences were based on aboveground and surface soil measurements only. The lack of soil-profile measurements reflects the expectation that the large heterogeneous belowground C pool
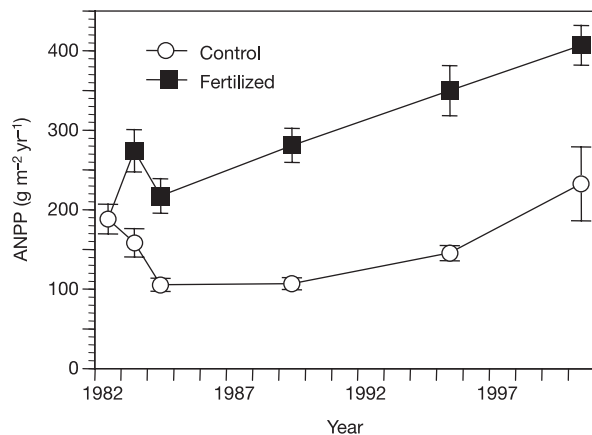

Figure 1 Effect of fertilization on vascular plant aboveground net primary production (ANPP) in tundra. Fertilized plots in moist acidic tundra near Toolik Lake, Alaska, have received $10\,g\,N\,m^{-2}\,yr^{-1}$ and $5\,g\,P\,m^{-2}\,yr^{-1}$ since 1981. Values are means (±1 standard error, s.e.); means from 1982–95 are reported in ref. 19; the year-2000 data are from this study ($n = 4$). Components of ANPP (new leaves and reproductive parts, new stems and secondary growth) are shown in Supplementary Fig. 1.